remote sensing

MDPI

Article

A Cross-Resolution Surface Net Radiative Inversion Based on Transfer Learning Methods

Shuqi Miao [1], Qisheng He [1,*], Liujun Zhu [2,3], Mingxiao Yu [1], Yuhan Gu [1] and Mingru Zhou [1]

[1] College of Geography and Remote Sensing, Hohai University, Nanjing 211100, China; 211301060003@hhu.edu.cn (S.M.); 211301060005@hhu.edu.cn (M.Y.); 221301060009@hhu.edu.cn (Y.G.); 221301050004@hhu.edu.cn (M.Z.)
[2] The National Key Laboratory of Water Disaster Prevention, Hohai University, Nanjing 210098, China; liujun.zhu@hhu.edu.cn
[3] Yangtze Institute for Conservation and Development, Hohai University, Nanjing 210098, China
* Correspondence: heqis@hhu.edu.cn

Abstract: Net radiation (Rn) is a key component of the Earth's energy balance. With the rise of deep learning technology, remote sensing technology has made significant progress in the acquisition of large-scale surface parameters. However, the generally low spatial resolution of net radiation data and the relative scarcity of surface flux site data at home and abroad limit the potential of deep learning methods in constructing high spatial resolution net radiation models. To address this challenge, this study proposes an innovative approach of a multi-scale transfer learning framework, which assumes that composite models at different spatial scales are similar in structure and parameters, thus enabling the training of accurate high-resolution models using fewer samples. In this study, the Heihe River Basin was taken as the study area and the Rn products of the Global Land Surface Satellite (GLASS) were selected as the target for coarse model training. Based on the dense convolutional network (DenseNet) architecture, 25 deep learning models were constructed to learn the spatial and temporal distribution patterns of GLASS Rn products by combining multi-source data, and a 5 km coarse resolution net radiation model was trained. Subsequently, the parameters of the pre-trained coarse-resolution model were fine-tuned with a small amount of measured ground station data to achieve the transfer from the 5 km coarse-resolution model to the 1 km high-resolution model, and a daily high-resolution net radiation model with 1 km resolution for the Heihe River Basin was finally constructed. The results showed that the bias, R^2, and RMSE of the high-resolution net radiation model obtained by transfer learning were 0.184 W/m^2, 0.924, and 24.29 W/m^2, respectively, which was better than those of the GLASS Rn products. The predicted values were highly correlated with the measured values at the stations and the fitted curves were closer to the measured values at the stations than those of the GLASS Rn products, which further demonstrated that the transfer learning method could capture the soil moisture and temporal variation of net radiation. Finally, the model was used to generate 1 km daily net radiation products for the Heihe River Basin in 2020. This study provides new perspectives and methods for future large-scale and long-time-series estimations of surface net radiation.

Keywords: net radiation; multi-scale transfer learning; deep learning; Heihe River Basin

Citation: Miao, S.; He, Q.; Zhu, L.; Yu, M.; Gu, Y.; Zhou, M. A Cross-Resolution Surface Net Radiative Inversion Based on Transfer Learning Methods. *Remote Sens.* **2024**, *16*, 2450. https://doi.org/10.3390/rs16132450

Academic Editor: Dusan Gleich

Received: 21 May 2024
Revised: 24 June 2024
Accepted: 30 June 2024
Published: 3 July 2024

1. Introduction

Net radiation (Rn) is a critical component of the Earth's energy balance [1], representing the net sum of incoming and outgoing shortwave and longwave radiation at the Earth's surface. It is essential for determining the energy balance of the Earth and maintaining the stability of the climate system. Net radiation plays a significant role in regulating surface temperatures and influencing climate patterns [2]. The formula for net radiation can be expressed as follows [3,4]:

$$R_n = R_{ns} + R_{nl} \quad (1)$$

$$R_n = R_s^{\downarrow} - R_s^{\uparrow} + R_l^{\downarrow} - R_l^{\uparrow} \quad (2)$$

$$R_n = (1 - \alpha) R_s^{\downarrow} + R_l^{\downarrow} - R_l^{\uparrow} \quad (3)$$

where R_{ns}, R_{nl}, $R_s^{\downarrow}$, $R_s^{\uparrow}$, $R_l^{\downarrow}$, and $R_l^{\uparrow}$ are the surface net shortwave radiation (W/m^2, where downward is defined as positive), net longwave radiation (W/m^2), downward shortwave radiation (W/m^2), upward shortwave radiation (W/m^2), downward longwave radiation (W/m^2), and upward longwave radiation (W/m^2). α is the surface broadband albedo.

In the realm of remote sensing, the precise measurement of net radiation holds substantial scientific significance for a comprehensive grasp of the surface energy balance, the formulation of energy balance models, and the evaluation of the effects of climate change on surface dynamics. Gao [5] examined the temporal and spatial patterns of net radiation and its influence on the evapotranspiration process in the Tibetan Plateau by combining satellite data with meteorological station observations. Their findings illuminated the seasonality and geographic spread of surface net radiation, which was vital for forecasting the trends and variations of evapotranspiration in the area. Moreover, Li [6] employed MODIS data to conduct systematic global monitoring and estimation of surface net radiation, uncovering its global distribution. This research not only offered essential data support for a deeper comprehension of the Earth's energy balance dynamics but also established a robust foundation for further global climate change analysis. Additionally, Meng [7] conducted numerical simulations to investigate the effects of urbanization on surface net radiation. The findings indicated that urbanization results in an increase in net surface radiation due to alterations in surface cover and albedo, which has substantial adverse impacts on urban climate and environmental quality. These outcomes enhance our understanding of the role of net surface radiation and offer a solid scientific foundation for assessing the shifts in the Earth's energy balance and climate system in the context of urban development.

Traditional net radiation measurement techniques mainly consist of direct in situ measurements and data collected by ground-based meteorological stations. However, the use of ground-based net radiation measurements faces many limitations due to the short observation duration and high maintenance costs [8]. Therefore, scholars have begun to investigate alternative methods of obtaining net radiation data using reanalysis and satellite-derived products, as shown in Table 1. Reanalysis merges existing observations with meteorological models to provide comprehensive datasets with extensive time coverage [9]. These datasets have the advantage of extended time series, but typically have coarser spatial resolution and are often less accurate than satellite data products [10]. This discrepancy may stem from the inaccuracy of cloud data [11,12]. In addition, while there are net radiation products derived from satellite observations, most lack the necessary spatial detail. The highest spatial resolution product currently available is the Global Land Surface Satellite (GLASS) [13], which has a resolution of only 0.05°, which is insufficient to capture spatial variations in the land surface. This limitation hinders the application of net radiation data on regional scales. Therefore, there is still a great demand for net radiation products that combine high accuracy and fine spatial and temporal granularity.

Currently, large-scale studies on net radiation inversion predominantly utilize a combination of satellite technology and terrestrial observational data. This field encompasses a range of research methodologies and technical tools, such as energy balance models [14], radiative transfer models [15], as well as machine learning [16] and deep learning algorithms [17,18]. The essence of the energy balance model is the formulation of the surface energy balance equation, which encapsulates the energy transfer processes between the surface and the atmosphere. This includes elements like solar irradiance, atmospheric radiation, thermal conduction, and convection. The model employs satellite data and meteorological surface observations to ascertain the essential parameters. Despite its robust theoretical underpinnings, the energy balance model's application is hindered by the extensive requirement for ground observations and the complexity of the modeling process [19]. Conversely, radiative transfer models leverage the principles of radiative

transfer, in conjunction with satellite data, to simulate the radiation interactions between the atmosphere and the Earth's surface. These models are capable of estimating key parameters such as surface albedo and temperature and, subsequently, the net radiation at the surface. In comparison to energy balance models, radiative transfer models exhibit greater adaptability and applicability, particularly in responding to environmental variations across diverse regions.

In recent years, the application of machine learning and deep learning techniques has demonstrated significant promise in the domain of net radiation inversion. These approaches analyze extensive datasets from both remote sensing and ground observations to create nonlinear models that connect net radiation with satellite data. By doing so, they adeptly capture intricate data patterns and trends, thereby enhancing the precision and dependability of net radiation forecasts. Machine learning techniques not only bolster the precision and efficiency of net radiation inversion through sophisticated data processing and analytical methods but they also offer a novel, agile, and efficient avenue for net radiation estimation, particularly within the context of big data environments. For instance, Zeng [20] harnessed deep learning to gauge net radiation, elaborating on the benefits of deep learning in integrating satellite and meteorological data and its potential for net radiation estimation. Li [21] introduced a machine learning-based data fusion strategy tailored to the Tibetan Plateau's intricate topography and climate, showcasing the efficacy of machine learning in estimating net radiation under such challenging conditions. Wang [22] presented a deep learning model for terrestrial net radiation estimation and compared its efficacy with conventional physical models, underscoring the deep learning model's superior generalization and accuracy. Liu [23] proposed a machine learning-based approach for estimating surface net solar radiation, applying it to a water energy balance model and discussing the model's potential in net radiation estimation and its application in water energy balance modeling. Zhang [24] put forth a deep learning-based method for deriving surface net radiation from satellite data, discussing the method's capacity to manage large-scale satellite data and enhance the precision of net radiation estimation.

Although machine learning and deep learning techniques have shown great potential in the field of surface net radiation inversion, improving estimation accuracy and enhancing model adaptation, there are still challenges in practical applications, such as the uneven distribution of surface flux observation stations, varying quality of ground data, and limitations in the resolution of remotely sensed data. However, as the need for a refined understanding of the surface energy balance and hydrological processes increases, so does the requirement for the spatial and temporal resolution of net radiation data.

Net radiation is the center of surface energy balance studies, and downscaling to improve its spatial and temporal resolution is crucial. In this context, the transfer learning approach, as an innovative deep learning method, has been shown to be effective in combining target data with field measurements to construct high-resolution models of surface parameters. Hemmati [25] conducted an in-depth study of soil moisture at the local scale by combining synthetic aperture radar (SAR) data with the transfer learning technique. The study not only confirmed the effectiveness of transfer learning in inverting soil moisture but also demonstrated its potential in modeling soil moisture with spatial and temporal resolution. In addition, Zhu [26] used Sentinel-1 data combined with a transfer learning model to successfully reduce the resolution of soil moisture data from 9 km to 0.1–1 km and verified the accuracy of transfer learning in inverting soil moisture in sample-scarce areas. Together, these findings demonstrate the reliability and applicability of the transfer learning approach in surface parameter inversion.

In this study, an innovative method is proposed to address the limitations of existing net radiation inversion methods. The method is based on a transfer learning framework and relies on a deep learning model of DenseNet, aiming to significantly improve the spatial–temporal resolution and inversion accuracy of net surface radiation using limited ground station measured data. This study established a 1 km high temporal and spatial resolution model of net surface radiation and evaluated the accuracy of the model estimation by

combining the station data and GLASS Rn products. The results of this study promote the development of the surface net radiation inversion technique and provide valuable experience and methodological guidance for subsequent related studies. In addition, the method realizes the spatial downscaling of the net radiation data, which provides solid technical support and a data basis for the in-depth study of the energy balance of the surface, the hydrological cycle, and the fine monitoring of environmental changes at the regional scale, among other applications.

Table 1. Table of available domestic and international net radiation products.

Type	Dataset	Spatial Resolution	Temporal Resolution	Time Span
Reanalysis Products	NCEP/CFSR [27]	38 km	6-hourly	1979–2010
	NASA/MERRA [28]	0.5° × 2/3°	hourly	1979–
	ERA40 [29]	125 km	6-hourly	1957–2002
	ERA-Interim [30]	80 km	3-hourly	1980–
	JRA55	55 km	3-hourly	1958–
	NVEP/NCAR RII	200 km	6-hourly	1979–
Remote Sensing Products	CERES-SYN [31]	1°	3-hourly	2000–
	ISCCP-FD [32]	280 km	3-hourly	1983–2011
	GLASS/Rn	0.05°	daily	2000–2020

2. Materials and Methods

2.1. Data Sourcing and Preprocessing

2.1.1. In Situ Measurements

The in situ measurement data used in this study were obtained from the Heihe integrated observatory network. The network is based on the Heihe River Basin Joint Telemetry Experimental Research (HiWATER) [33,34], and the observatories cover a wide range of surface types such as farmland, grassland, woodland, wetland, desert, bare ground, and sandy land, in order to achieve the comprehensive monitoring of surface processes under different surface cover conditions. The locations and detailed information of the stations are shown in Figure 1 and Table 2.

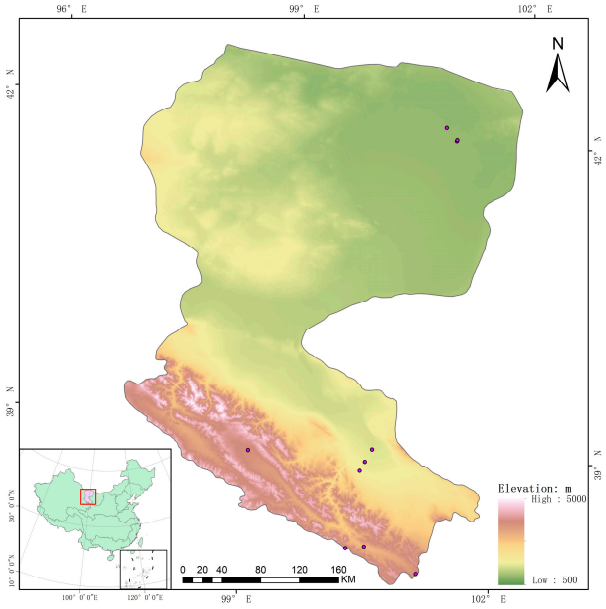

Figure 1. Elevation information for the study area and spatial distribution of eddy flux observatories (dots indicate observatories).

Table 2. Table of locations and details of field measurement sites.

Station	Longitude/°E	Latitude/°N	Elevation/m	Type
A' rou	100.4643	38.0473	3033	Grassland
Daman	100.3722	38.8555	1556	Cropland
Dashalong	98.9406	38.8399	3739	Grassland
Huazhaizi	100.3201	38.7659	1731	Desert
Desert	100.9872	42.1135	1054	Desert
Mixed forest	101.1335	41.9903	874	Mixed forest
Jingyangling	101.116	37.8384	3750	Grassland
Sidaoqiao	101.1374	42.0012	873	Shrubs
Yakou	100.2421	38.0142	4147	Grassland
Zhangye wetland	100.4464	38.9751	1460	Wetland

2.1.2. NDVI Remote Sensing Datasets

In this study, we used normalized difference vegetation index (NDVI) products from Fengyun-3 satellites with a spatial resolution of 250 m and 1 km and a temporal resolution of 10 days and monthly, which enriched our understanding of surface vegetation conditions. These data are distributed through the Feng Yun Satellite Remote Sensing Data Service (https://satellite.nsmc.org.cn, accessed on 1 March 2024) and stored in HDF format, covering global attribute information, scientific datasets, and virtual data. Twelve data layers are contained under each HDF file, including 10 days of synthetic albedo and bright temperature at a 1 km resolution (6 channels); 10 days of synthetic NDVI, zenith, and azimuthal angle information from the Sun and satellites; and vegetation index quality codes. This study provides accurate indicators for monitoring surface vegetation and contributes to an in-depth analysis and understanding of vegetation changes and their impact on net radiation.

2.1.3. GLASS Rn Datasets

This study used Global Land Surface Satellite (GLASS) remote sensing products provided by the University of Maryland (http://www.glass.umd.edu, accessed on 1 March 2024). This dataset provides a valuable data resource for the application of remote sensing technology in environmental monitoring by integrating key surface parameters such as downward shortwave radiation (DSR) and net radiation (Rn). The continuous decades of time series data provided not only have high accuracy but also achieve global coverage. In addition, a study by Jiang [35] further confirmed the accuracy of the GLASS Rn product through a validation exercise conducted at 142 stations around the world. In the validation study, the coefficient of determination (R^2) of the GLASS Rn product reached 0.80 and the root mean square error (RMSE) was 51.35 W/m^2, which is a result that fully demonstrates the reliability and validity of the GLASS dataset in the construction of net radiation models.

2.1.4. Meteorological Datasets

In this study, the "China Meteorological Administration Land Data Assimilation System (CLDAS-V2.0) real-time product dataset" (http://data.cma.cn, accessed on 1 March 2024) was adopted. The dataset covers the entire Asian region from 0° to 65° N latitude and 60° to 160° E longitude, with a spatial resolution of 0.0625° × 0.0625° and temporal resolution options of hourly and daily, and all the data are based on an isotropic latitude/longitude grid for integration and analysis. In data processing and analysis, the dataset adopts advanced techniques such as Multi-Grid Variational Assimilation (MGV) and Optimal Interpolation (OI) to ensure high-quality and spatial–temporal resolution in the China region.

The CLDAS dataset has been updated in real time since 2008 and integrates six key elements of the atmospheric dynamical field, including air temperature and specific humidity at 2 m altitude, wind speed at 10 m altitude, precipitation, shortwave radiation,

and surface air pressure. In addition, the dataset includes a rich set of products such as ground temperature analysis, multilayer analysis of soil temperature and humidity, detailed data on soil temperature (five layers of 5, 10, 40, 100, and 200 cm) and humidity (five layers of 0–5, 0–10, 10–40, 40–100, and 100–200 cm), and soil relative humidity (three layers of 0–10 cm, 0–20 cm, and 0–50 cm). The dataset is updated in real time with a delay of 30 min for meteorological elements (temperature, barometric pressure, humidity, and wind speed), 50 min for shortwave radiation, 1.5 h for precipitation data, and 2 days for near-real-time products. This study paid special attention to the atmospheric dynamic field data in the dataset, focusing on specific humidity (SHU), pressure (PRS), wind speed (WIN), temperature (TEMP), and shortwave radiation (SSRA).

2.2. Model Design

2.2.1. Sample Production

The aim of this study was to achieve knowledge transfer from 5 km coarse-resolution to 1 km high-resolution net radiation models. To this end, the process of preparing the model training samples involved careful preprocessing work on the input variable x, and its corresponding target truth value at 5 km and 1 km resolution y was carefully preprocessed. The remote sensing dataset used in this study contained multiple variables that underwent preprocessing steps including outlier removal, data interpolation, and resampling to ensure that pixel-level-matched sample datasets were obtained.

Although the Eddy-Pro software executed preliminary processing of the observed data from the monitoring stations [36,37], the actual net radiation output values from the monitoring stations could contain missing data, usually expressed as -6999, due to factors such as instrument failures and data quality control. In the process of constructing the net radiation transfer learning model, these data needed to be further cleaned and processed to filter out the daily average net radiation values with more complete data for model construction, while excluding those records with more missing data. The recovery of missing net radiation data through interpolation was necessary in the calculation of daily averages, and records with more than one-sixth of the total number of days of missing daily data needed to be excluded to minimize errors and ensure that only high-quality data were used for the construction of the transfer learning model.

In order to balance the order-of-magnitude differences between the input variables, this study introduced a normalization technique in the early stages of model construction. The purpose of normalization was to enhance the model's ability to capture the characteristics of each variable and improve the efficiency of the underlying model training and simulation. As shown in Table 3, all the sample data and their maximum and minimum values for each variable were listed to ensure that the treatments covered all possible scenarios for the region. In particular, for the variable date (DOY), whose periodicity feature was not suitable to be directly represented by linear coding, a special normalization method was adopted: firstly, DOY was normalized to the range of $-\pi$ to π and then subsequently converted to a range between 0 and 1 by the cosine transform, which enabled the model to accurately capture the periodicity feature of date. With this normalization, the input features of the model were further optimized, providing a solid foundation for efficient and accurate transfer learning.

In this study, we aimed to achieve knowledge migration from a coarse model at 5 km resolution to a highly refined model at 1 km resolution. For this purpose, we first selected all image elements with a 5 km resolution from multi-source remote sensing datasets from 2017 to 2019. In the face of the large number of samples, we adopted a random sampling method to select 1,000,000 samples, which constituted the base dataset for coarse model training and were used to train the coarse model with 5 km spatial resolution. In addition, a limited number of 6094 new samples with 1 km spatial resolution were generated using data from ground-truthing stations. We hoped to fine-tune the parameters of the pre-trained coarse model with the high-resolution samples in order to improve the spatial resolution of the model while maintaining or improving the prediction accuracy.

Table 3. Table of sample variables as well as standardized information.

Type	Variable Name	Minimum	Maximum	Unit	Time Span
Time	DOY	1	365		
Locations	5 km grid longitude	97.1	101.95	D	
	5 km grid latitude	37.7	42.7	D	
Vegetation descriptors (FY-3)	NDVI	−1	1		2018–2020
Climate variables (CLDAS 2.0)	PRS	0	113.15	kPa	2018–2020
	SHU	0	0.03	kg/kg	
	SSRA	−200	500	W/m^2	
	WIN	0	20	m/s	
	TAVG	0	350	K	
	TMIN	0	350	K	
	TMAX	0	350	K	

2.2.2. Dense Convolutional Network for Net Radiation

In this study, we adopted the dense convolutional network (DenseNet) model proposed by Huang [38] in 2017, which optimized the network architecture through an innovative dense connectivity mechanism for the efficient transfer of information between layers. This design greatly improves the mobility and reusability of features and effectively mitigates the common gradient vanishing problem in deep learning. The architecture of DenseNet allows each layer of the network to directly receive the feature maps of all layers of the previous sequence, thus enhancing the model's learning ability and feature propagation efficiency. In addition, DenseNet effectively reduces the risk of overfitting by reducing the number of parameters and increasing the efficiency of parameter usage. The flexibility of DenseNet lies in the tunability of its network depth and growth rate, which allows it to be customized and configured according to the specific dataset and task requirements, which is especially important for parsing complex radiometric data. Therefore, DenseNet is considered ideal for capturing subtle patterns and complex relationships in radiation data, promising to improve prediction accuracy and optimize model training efficiency. Aljazaeri [39] verified that the DenseNet model has higher accuracy in linear regression; Zhu [26] also used the DenseNet model to successfully predict soil moisture data, which verified the superiority of the model in regression prediction.

In this study, a deep learning model based on the DenseNet architecture was constructed with the aim of inverting radiometric data at high spatial resolution using inverse learning techniques, as shown in Figure 2. The input feature set of the model contained multidimensional features such as meteorological data, NDVI, date, and locations, which were appropriately preprocessed to fit the model. In the model structure, each dense block consisted of three fully connected layers with batch-normalized and rectified linear unit (ReLU) activation functions. To facilitate feature reuse and improve parameter efficiency, this study introduced a shortcut connection mechanism that connected the input of each dense block to its output. The outputs of these dense blocks were subsequently connected to a fully connected layer containing 32 neurons and ultimately output the predicted value of the net radiance value through a single neuron output layer. In the DenseNet model, the number of neurons (w) and the number of dense blocks (d) were two key hyper-parameters that determined the width and depth of the model, respectively.

During the model training process, we adopted the Adam optimization algorithm with mean square error (MSE) as the loss function to guide the updating and optimization of model weights. In order to fully utilize the pre-training samples, we first pre-trained the model on a large-scale dataset (5 km) based on GLASS Rn data as the target data to learn a generic feature representation and then fine-tuned the model for a small-scale dataset (1 km) with in situ measured net radiation data as the new target data. In addition, in order to improve the prediction accuracy and generalization ability of the model, this study

employed an integration learning strategy, which enhanced the robustness of the model by integrating the prediction results from multiple independent models and reducing the uncertainty and variance of the predictions. For performance evaluation, we divided the data into an 80% training set and a 20% test set. The training set contained pre-trained samples, while the test set was specialized for radiometric data at 1 km resolution. By calculating key metrics such as the deviation between the predicted and actual values of the model for the test set, correlation coefficients, and root mean square errors, we are able to comprehensively evaluate the model's prediction performance on the 1 km samples. These evaluation results not only demonstrated the generalization ability of the model but also reflected its accuracy and robustness in dealing with high-spatial-resolution data.

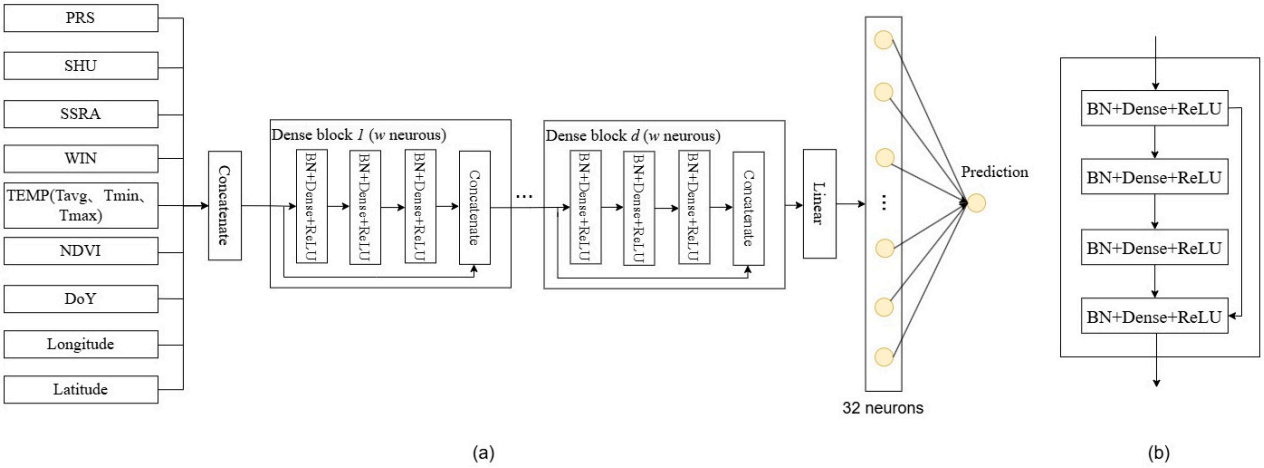

Figure 2. Structure of the densely connected network (**a**) and dense blocks (**b**). BN, Dense, and ReLU in the figure are the fully connected dense layer and the bulk normalized activation layer ReLU, respectively. The model contained d dense blocks with w neurons in each dense layer. The input data were fed into the model in a sequential manner, with each input record containing 11 values, which were processed one by one in a given order.

2.2.3. Ensemble Transfer Learning Framework

As shown in Figure 3, this study was based on a transfer learning approach, the core idea of which was to build models for high-resolution net radiation data based on the DenseNet model architecture. The starting point was the assumption that effective knowledge transfer could be established between deep neural networks trained for 5 km coarse resolution and 1 km high-resolution net radiation models by sharing similar model architectures and training parameters. To this end, we first pre-trained a 5 km coarse-resolution base model using GLASS net radiation data and used this to build a 5 km resolution regional net radiation model of the Heihe River Basin as a starting point for the transfer learning process. Through this approach, we aimed to achieve accurate prediction from low- to high-resolution data, thus improving the generalization ability of the model at different spatial scales.

Considering that the available 5 km data provided a sufficient sample size, this opened up the possibility of training depth and breadth models, which is in line with the findings of Eldan [40] and Wu [41] that an increase in the depth and breadth of a model contributes to improved model performance. However, such high-performance low-resolution models are not guaranteed to maintain the same level of accuracy when migrating to high-resolution targets, especially in high-resolution scenes where samples are scarce. To address this challenge, instead of directly pursuing the optimal model width (w), depth (d), or other hyper-parameters, this study chose to train a series of DenseNet models with different widths and depths at a resolution of 5 km, with the widths w set to 8, 16, 32, 64, and 128 and the depths d set from 1 to 5. This produced a total of 25 DenseNet models with different trainable parameter configurations.

This resulted in a total of 25 DenseNet models with different trainable parameter configurations, ranging from the simplest DenseSM-1-8 model to the most complex DenseSM-5-128 model.

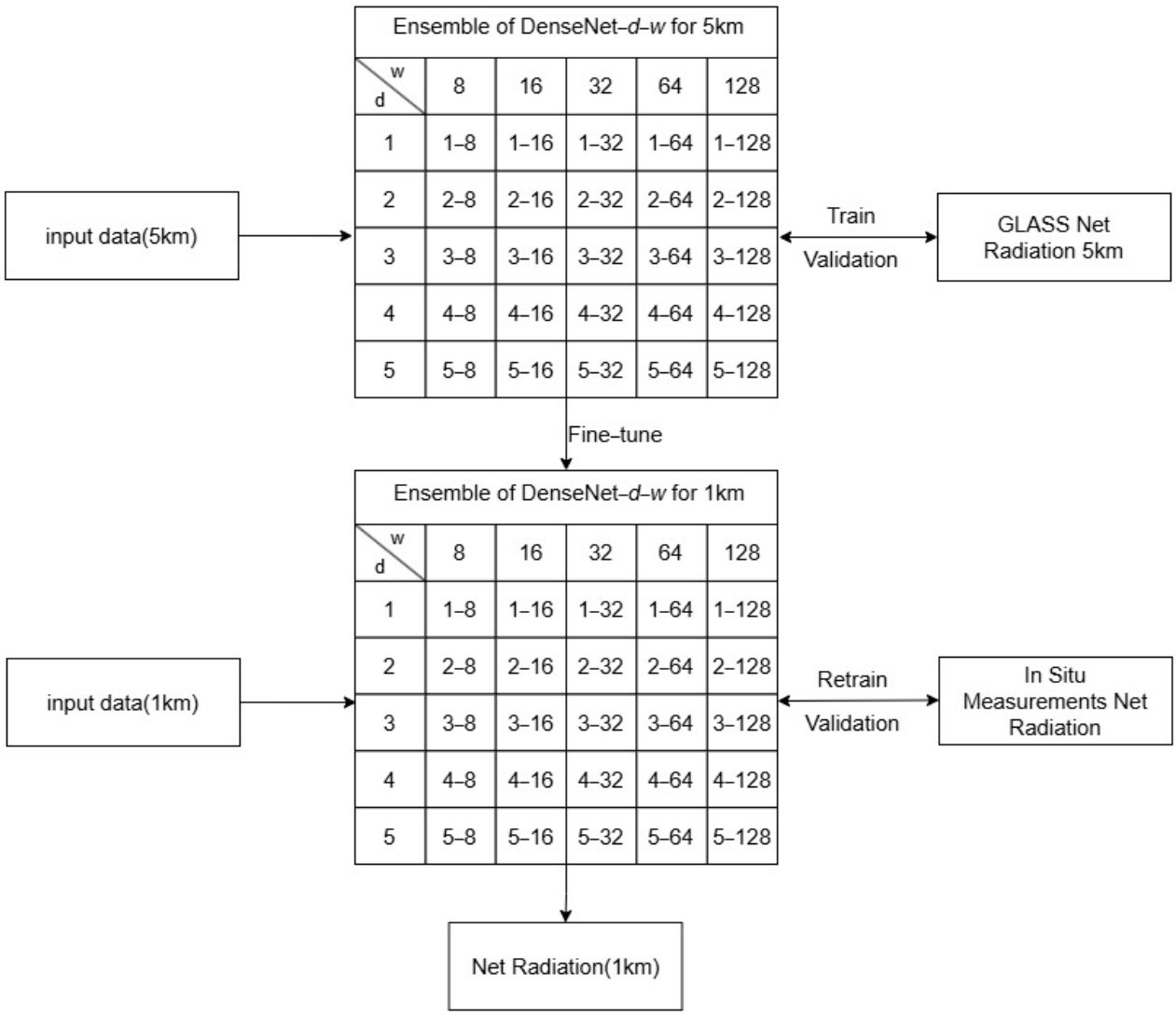

Figure 3. A net radiative transfer learning framework based on dense convolutional networks was implemented to optimize 25 densely connected networks for 1 km net radiative inversion by a fine-tuning method. In the figure, *d* and *w* refer to the number of densely connected blocks and the number of neurons, respectively.

During the training of the coarse resolution models, 80% of the data was used as the training set and the remaining 20% was used for validation. The models were trained using the root mean square error (RMSE) as the loss function and the Adam optimizer, with parameters set to $\beta 1 = 0.9$, $\beta 2 = 0.999$, and $\epsilon = 10^{-8}$. In order to balance the accuracy and efficiency of the training, we set up 128 batches and set the learning rate to 0.01. Each model was trained for 100 cycles, of which the last 10 cycles of the model states were averaged to form a so-called model snapshot set. This strategy helped to build more stable and reliable predictive models. With this integrated approach of model complexity and training strategy, this study aimed to achieve an effective transfer from low- to high-resolution data, which, in turn, improved the prediction performance of the models at different spatial scales.

In the transfer process to higher resolutions, we performed fine-tuning of 25 fully trained low-resolution models for the prediction task of high-resolution net radiation data. The fine-tuning process was designed to allow the models to adapt to new tasks that

were different from the original training tasks by using fewer samples and reducing the learning rate. In this process, we used a smaller learning rate of 1×10^{-5} and trained each low-resolution model for an additional 1000 cycles to optimize its prediction performance on high-resolution data. Notably, during the fine-tuning process, we kept the other training settings consistent, including the model snapshot ensemble strategy for the last 10 cycles, which helped ensure model stability and convergence during training. With this approach, we were able to efficiently estimate the net radiance data at high resolution. With this combined fine-tuning and integrated learning strategy, this study aimed to achieve an effective transfer from low- to high-resolution data, which, in turn, improved the prediction performance and reliability of the model at different spatial scales.

2.2.4. Methodology

The workflow of this study is shown in Figure 4 and included the following steps: firstly, pre-processing of the raw data, including filtering, interpolation, and outlier rejection, was performed to ensure the temporal and spatial integrity of the data, and second, image element resampling was performed to achieve inter-image consistency, the GLASS Rn product was used to generate the original training samples(1,000,000) with 5 km resolution, and a new training sample with 1 km resolution was generated by combining training samples with the limited ground-truthing data (6094). The sample data were then partitioned at 80% (training) and 20% (validation) to support model training and validation. Further, based on the DenseNet architecture, 25 deep learning models were constructed to integrate multi-source data to learn the spatio-temporal distribution features of the GLASS Rn products, and a net radiation model with a 5 km resolution was trained. Then, the pre-trained models were fine-tuned using a small amount of ground truth data to achieve the model conversion from 5 km to 1 km resolution, and a 1 km resolution daily net radiation model was constructed for the Heihe River Basin. Finally, the daily high-resolution net radiation model obtained by migration learning was evaluated and a 1 km spatial resolution net radiation product for the Heihe River Basin was generated, which was compared with the original GLASS Rn data to validate the accuracy of the model and initially applied to the product generation.

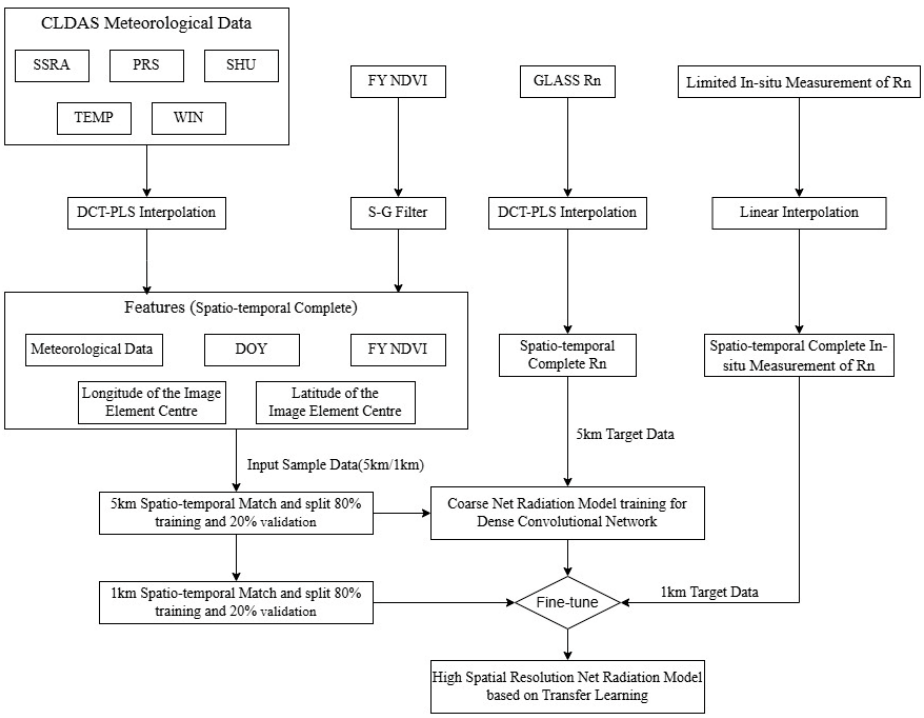

Figure 4. Flowchart of this study.

2.3. Model Evaluation Metrics

In this study, in order to comprehensively evaluate the performance of model training, we used four key statistical metrics: mean bias (*bias*), coefficient of determination (R^2), root mean square error (*RMSE*), and unbiased RMSE (*ubRMSE*). Each of these metrics provided a different perspective on the predictive accuracy and reliability of the model, as defined below:

$$bias = \frac{1}{n}\sum_{i=1}^{n}\left(Y_i - \hat{Y}_i\right) \tag{4}$$

$$R^2 = 1 - \frac{\sum_{i=1-1}^{n}\left(Y_i - \hat{Y}_i\right)^2}{\sum_{i=1-1}^{n}\left(Y_i - \overline{Y}_i\right)^2} \tag{5}$$

$$RMSE = \sqrt{\frac{1}{n}\sum_{i=1}^{n}\left(Y_i - \hat{Y}_i\right)^2} \tag{6}$$

$$ubRMSE = \sqrt{RMSE^2 - bias^2} \tag{7}$$

where Y_i, $\hat{Y}_i$, and $\overline{Y}_i$ represent the ith observation, model prediction, and mean of the observations, respectively, and n represents the number of observations.

3. Results

3.1. Evaluation of Pre-Trained Coarse-Resolution Net Radiation Models

In this study, to construct a coarse-resolution net radiation model, we designed a series of models with different depths d and widths w for a total of 25 models. The training results of these models are shown in Figure 4, from which it is found that all the coarse-resolution models exhibited small deviations in the training and validation phases, and the deviation values were distributed in the range of 0 to 1. In addition, the predictions of the 25 coarse-resolution models had high accuracy, which indicated that the coarse models were trained properly without over-fitting or under-fitting. As expected, both training and validation accuracies improved when w and d were increased, confirming that larger models were more powerful when sufficient training samples were available.

In this study, 25 coarse-resolution network radiation prediction models were constructed, of which the lowest performance was that of the DenseNet-1-8 model, which was particularly exceptional due to its shallower network structure and narrower network width. During the training phase, this model had a bias value of 0.46, clearly indicating a significant difference between the predicted values and the true observations. Despite the weak performance, the correlation coefficient R^2 reached 0.873, indicating that even a poorly performing model can reveal to some extent the correlation between input data and net radiance output. In addition, the RMSE and ubRMSE were 27.637 W/m^2 and 27.677 W/m^2, respectively, which were basically the same, indicating that the model prediction errors were mainly caused by random errors rather than systematic biases. With the increase of the model depth and width, the performance was obviously improved, especially for the DenseNet-4-128 model, where the bias was sharply reduced to 0.1, which was close to zero, indicating that the predicted values were very close to the real values. The correlation coefficient R^2 of the model was improved to 0.977, showing an extremely high prediction consistency, which further validated the effectiveness of the model in the field of net radiation estimation. Both the RMSE and ubRMSE were reduced to 12.004 W/m^2, reflecting a significant improvement in the model prediction accuracy and a substantial reduction in the error. However, it is worth noting that although DenseNet-4-128 performed the best in this study, the performance improvement was not significant as the model depth and width were further increased, suggesting that the performance reached a saturation point where further increases in model complexity no longer improved the performance significantly but only increased the computational resource consumption.

In this study, the robustness of coarse-resolution net radiation models in resolving the complex interactions between 5 km resolution meteorological data, key input parameters

such as vegetation indices, and GLASS Rn net radiation products was verified through metrics assessment. These models not only accurately captured the spatial and temporal distribution characteristics of the GLASS products but also demonstrated their potential application in simulating these distributions. Although the training accuracy of the current models was limited by the upper accuracy limit of the GLASS net radiation products and failed to exceed their learning objectives, the models accumulated a great deal of valuable knowledge about net radiation estimation in the process. In particular, by analyzing the GLASS net radiation data, the model gained the ability to resolve complex links between meteorological data and key input parameters such as vegetation indices.

3.2. Evaluation of High-Resolution Net Radiation Models for Fine-Tuning Transfer Learning

A group of coarse-resolution net radiation models were constructed based on a dense connectivity network, combining the idea of transfer learning by inputting 1 km input data and in situ measured data into the pre-trained coarse model, achieving the purpose of transfer learning by fine-tuning the model parameters. Finally, the daily net radiation data at 1 km resolution for the Heihe River Basin were generated.

According to Figure 5, the transfer learning model demonstrated substantial advantages in the accuracy of net radiation estimation. The RMSE and ubRMSE of the transfer learning model were 24.293 W/m^2 and 24.292 W/m^2, respectively, which showed a substantial reduction compared to the RMSE of the directly validated pre-trained coarse model of 42.94 W/m^2 as well as the RMSE of the GLASS Rn product of 35.741 W/m^2. This result directly proved the effectiveness of the transfer learning model in improving prediction accuracy. The correlation coefficient (R^2) of the transfer learning model was as high as 0.924, which not only exceeded the value of 0.758 for the pre-trained model but was also higher than the value of 0.839 for the GLASS Rn product. These data further confirmed the advantage of the transfer learning model in terms of its generalization ability, indicating that the model could better adapt to different datasets and environmental conditions. The fitting line of the transfer learning model was closer to the ideal 1:1 line, which indicated that there was less discrepancy between the model's predicted values and the actual observed values, thus validating the accuracy of the model prediction. In addition, the bias value of the transfer learning model was 0.184 W/m^2, which was much lower than the bias values of the pre-trained models (3.656 W/m^2 and -8.166 W/m^2), which showed the strong capability of the transfer learning model in reducing systematic bias.

As shown in Figure 6, the time-series plot combines the time-series curves between the net radiation data from GLASS, the net radiation data from the transfer learning inversion, and the net radiation data from the in situ measurements at different sites. It shows that the transfer learning was able to provide accurate estimates of net radiation for various land cover types, and the predictions were highly consistent with the trend of field observations, proving its accuracy and providing stable estimates under different environmental and climatic conditions, showing its robustness. In addition, the transfer learning model showed higher predictive performance compared to the multi-site GLASS Rn product, especially in capturing local variations and details of net radiation.

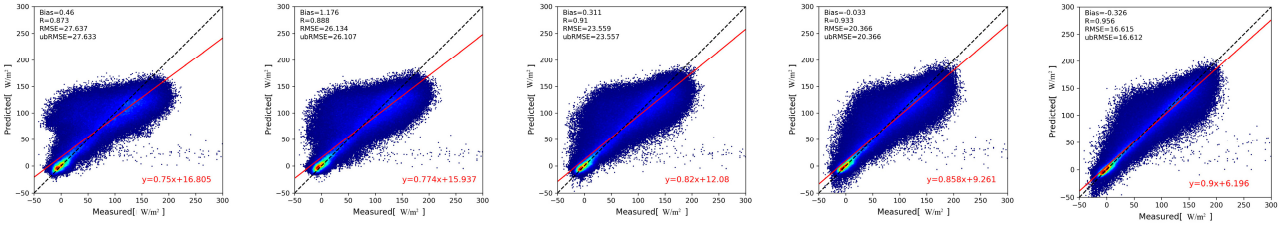

(**a**) (**b**) (**c**) (**d**) (**e**)

Figure 5. *Cont.*

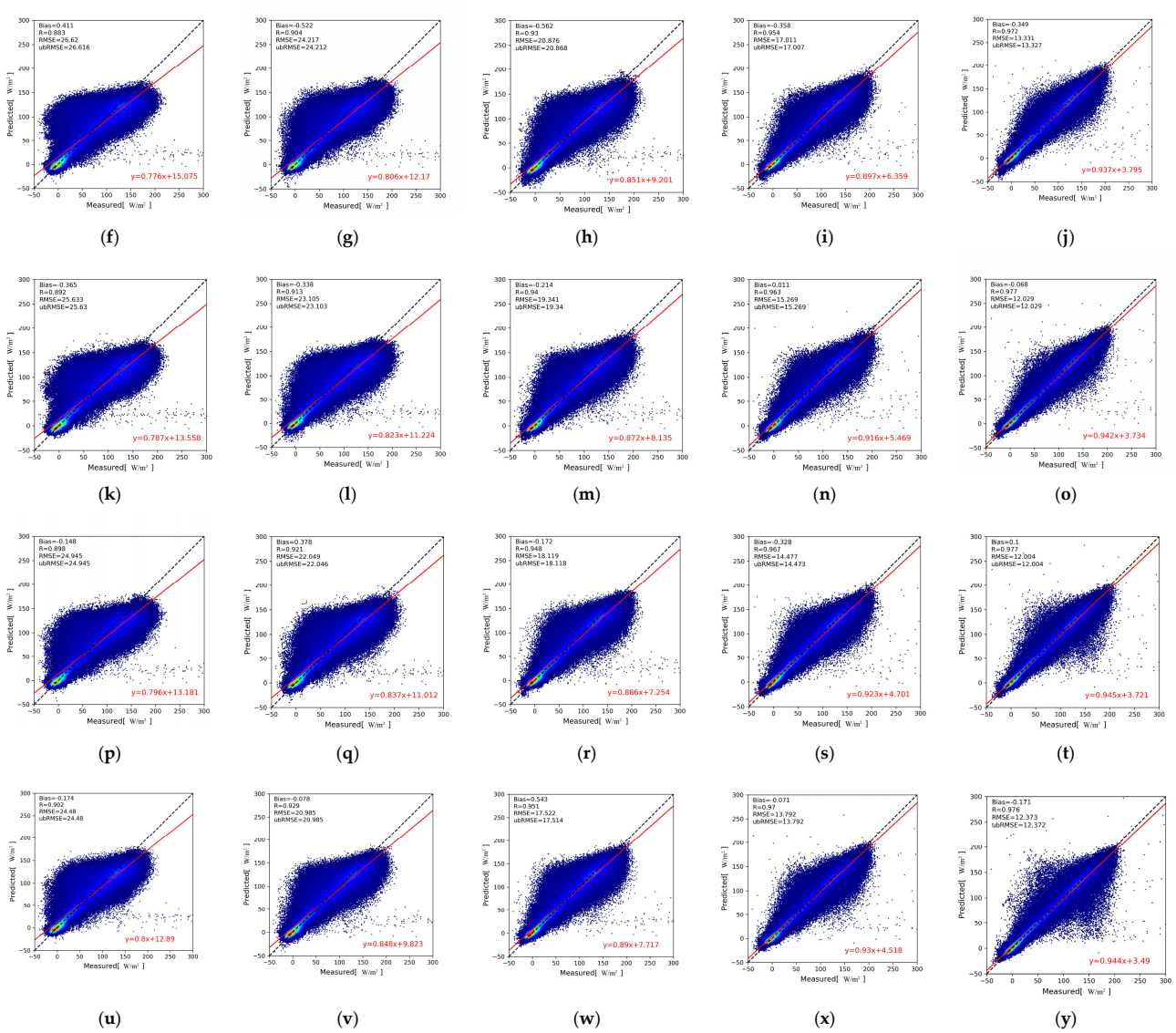

Figure 5. Training accuracy of 25 coarse resolution models, with based d(1, 2, 3, 4, 5) and w(8, 16, 32, 64, 128) being the number of dense blocks and the width of each dense layer. (**a**) DenseNet−1−8; (**b**) DenseNet−1−16; (**c**) DenseNet−1−32; (**d**) DenseNet−1−64; (**e**) DenseNet−1−128; (**f**) DenseNet−2−8; (**g**) DenseNet−2−16; (**h**) DenseNet−2−32; (**i**) DenseNet−2−64; (**j**) DenseNet−2−128; (**k**) DenseNet−3−8; (**l**) DenseNet−3−16; (**m**) DenseNet−3−32; (**n**) DenseNet−3−64; (**o**) DenseNet−3−128; (**p**) DenseNet−4−8; (**q**) DenseNet−4−16; (**r**) DenseNet−4−32; (**s**) DenseNet−4−64; (**t**) DenseNet−4−128; (**u**) DenseNet−5−8; (**v**) DenseNet−8−16; (**w**) DenseNet−5−32; (**x**) DenseNet−5−64; (**y**) DenseNet−5−128. The different color lines represent different meanings, there are 1:1 lines, and fitting lines, through the two lines, you can determine the effectiveness and accuracy of the model training.

As shown in Figures 7 and 8, comparing the 5 km resolution GLASS Rn product with the 1 km resolution Rn product based on transfer learning, the transfer learning model showed obvious advantages in improving the spatial resolution. The 1 km resolution data not only enhanced the ability to capture the heterogeneity of the ground surface but also revealed smaller spatial features, which is particularly important for regions with complex terrain and diverse ecosystems. This high-resolution output not only enhances the ability to identify changes in surface cover and topography but is also essential for modeling hydrological cycles, energy flows, and ecosystem dynamics.

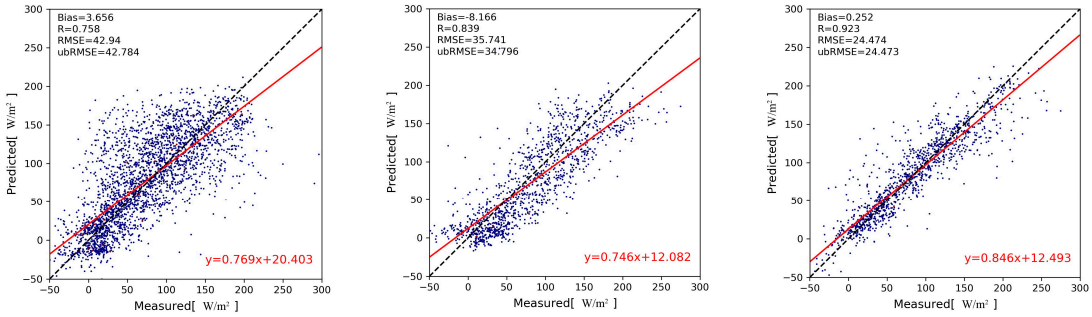

Figure 6. Scatter plots of net radiation estimation accuracy. (**a**) Pre-trained coarse model site validation scatter plot of accuracy. (**b**) GLASS Rn product site validation scatter plot of accuracy. (**c**) Fine-tuned transfer learning model site validation scatter plot of accuracy.

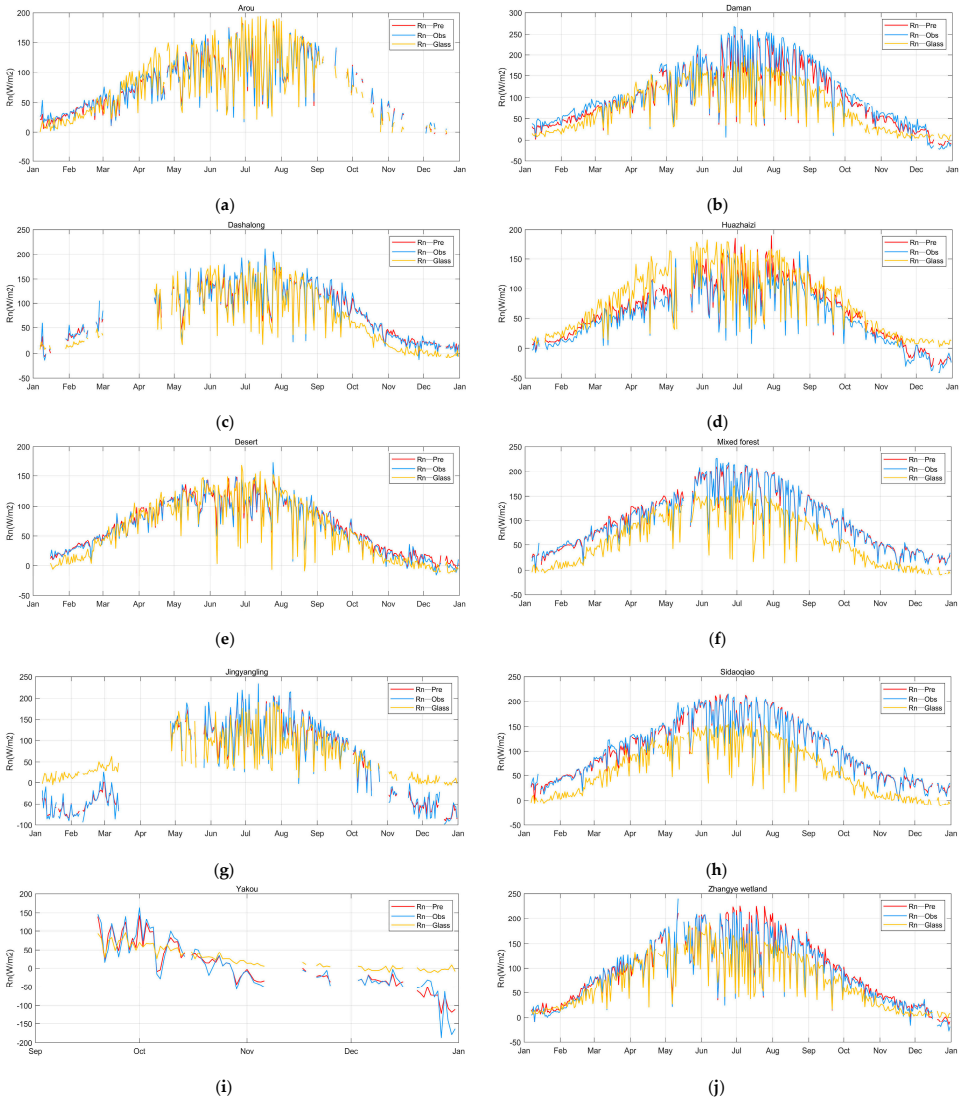

Figure 7. Time series plot of Rn with GLASS using in situ measurements at sites and based on fine-tuning transfer learning approach. (**a**) A'rou station (Grassland); (**b**) Daman (Cropland); (**c**) Dashalong station (Grassland); (**d**) Huazhaizi station (Desert); (**e**) Desert station (Desert); (**f**) Mixed forest station (Mixed forest); (**g**) Jingyangling station (Grassland); (**h**) Sidaoqiao station (Shrubs); (**i**) Yakou station (Grassland); (**j**) Zhangye wetland station (Wetland).

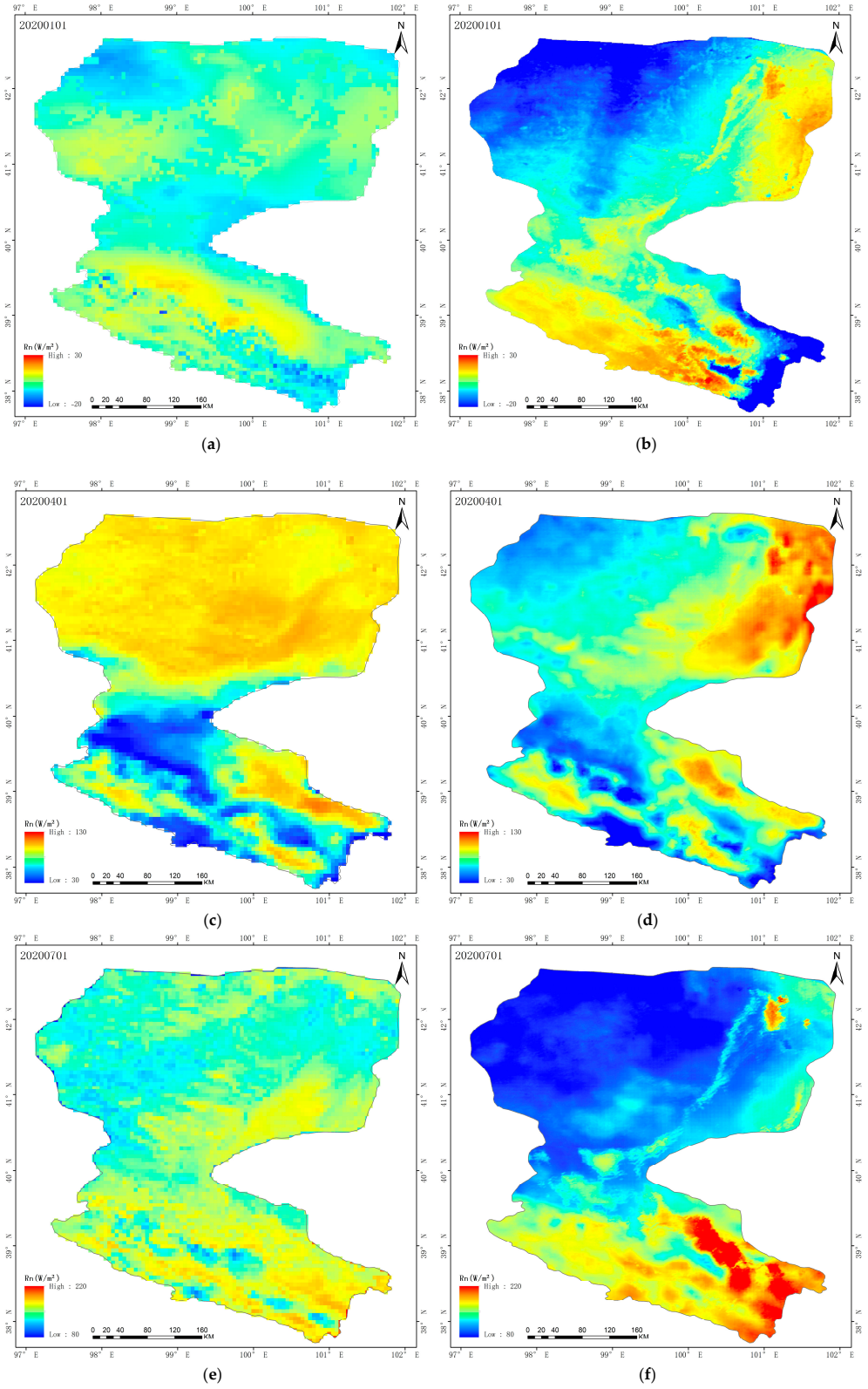

Figure 8. *Cont.*

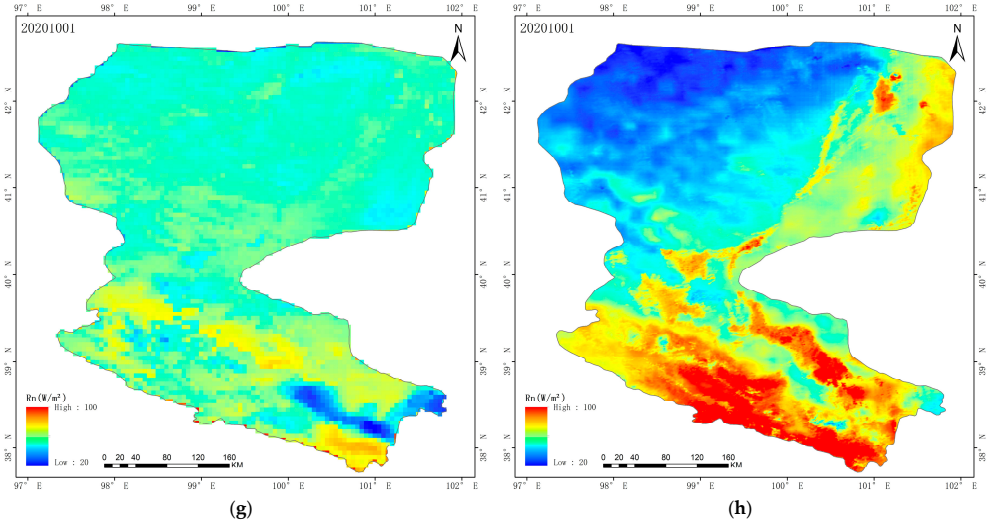

Figure 8. Spatial distribution of 2020 net surface radiation in the Heihe River Basin. Figures (**a**,**c**,**e**,**g**) show GLASS Rn products; figures (**b**,**d**,**f**,**h**) show net radiation products based on transfer learning.

3.3. Relative Importance of Features

Figures 9 and 10 illustrates the 2020 feature replacement importance analysis for transfer learning models based on validation data. Compared to traditional impurity-based approaches, replacement importance assessment avoids preference for rare features, provides a more objective measure of feature contribution, and can be dynamically calculated based on the validation dataset [42]. The feature importance assessments involved in this study were executed at a spatial resolution of 1 km to ensure consistency and the horizontal comparability of results. Shortwave radiation (SSRA) was the most critical variable in the constructed net radiation model [43,44]. Shortwave radiation is directly related to the amount of solar radiation received at the surface and is the main driver affecting the surface energy balance and net radiation calculations. Since shortwave radiation plays a central role in the energy exchange between the surface and the atmosphere, it occupies a pivotal position in net radiation estimation. When further analyzed, interactions between shortwave radiation and other meteorological elements, including maximum temperature (TMAX), average temperature (TAVG), minimum temperature (TMIN), and precipitation (PRS), may have a compounding effect on net radiation estimation [45]. For example, precipitation may indirectly affect the reception of shortwave radiation by changing cloud conditions and atmospheric transmittance. In addition, surface albedo and vegetation cover may also affect net radiation by regulating the absorption and reflection of solar radiation from the surface [46,47].

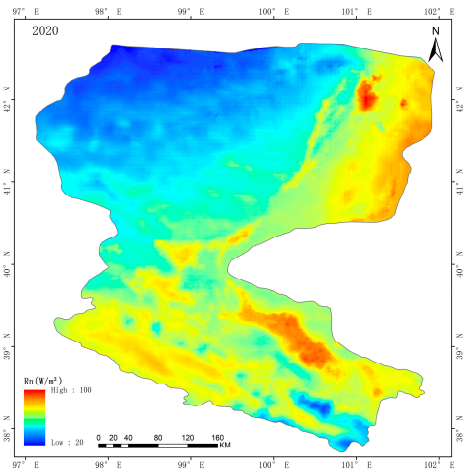

Figure 9. Spatial distribution of daily average surface net radiation in the Heihe River Basin in 2020.

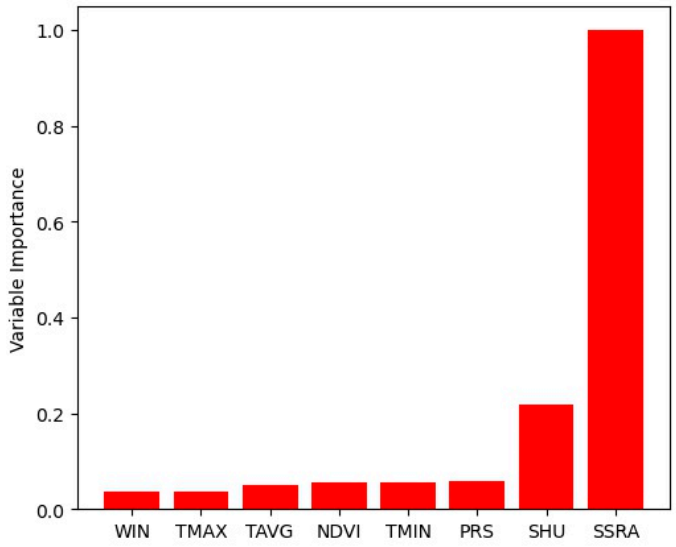

Figure 10. Relative importance of net radiation model predictors.

4. Discussion

This study proposes a framework for constructing high-temporal- and spatial-resolution net radiation models by transfer learning. Machine learning or deep learning can be directly used to invert net radiation. For example, Xu [48] used a deep learning approach combined with a statistical method to invert sea surface longwave radiation and verified the accuracy of the product. However, direct inversion requires a large amount of ground truth data to train the model to ensure the accuracy of the model [49]. However, the small and spatially uneven distribution of currently available in situ measurements and the high cost of establishing in situ measurement stations make it difficult to construct high-resolution net radiation models based directly on in situ measurements while ensuring the accuracy of the models. In contrast, transfer learning is an efficient machine learning technique that improves learning efficiency and model performance by applying knowledge learned from one task to another reconnected task. The advantages of this approach are improved data utilization efficiency, an accelerated learning process, enhanced model generalization capability, reduced computational costs, reduced dependence on large amounts of training data, improved stability of the training process, and enhanced model adaptability and immunity to new data distributions [50–52].

Therefore, in this study, a robust pre-trained model with 25 coarse resolutions (5 km) was constructed based on the transfer learning framework of the DenseNet model to learn the distribution pattern of GLASS Rn products in time and space. The training results are shown in Figure 5. However, despite the high training accuracy of the coarse model, the model was unable to outperform the product itself [53], and inherited the uncertainty of the GLASS Rn product. Therefore, in this study, the coarse-resolution model parameters were fine-tuned using the measured data from the stations, and the construction of a high-temporal- and spatial-resolution surface net radiation model was realized by migrating knowledge from the coarse-resolution model to the high-resolution model, and the upper bias, R^2, and RMSE of the simulation accuracies of the high-resolution net radiation model obtained by migratory learning were 0.184 W/m^2, 0.924, and 24.29 W/m^2.

The GLASS Rn product was selected as the target data source for the coarse model in this study due to the fact that it provides accurate net radiation estimates for both low and high mid-latitudes through the fusion of the two algorithms [54]. The GLASS Rn product exhibits a root mean square error (RMSE) of 51.24 W/m^2, which is a higher accuracy compared to the 54.96 W/m^2 of CERES [13,48]. In addition, the GLASS Rn product has a spatial resolution of up to 0.05°, which can provide continuous long-term net surface radiation data, which is essential for climate change studies and surface energy balance

analysis. Guo [55] further verified the advantage of the GLASS Rn product over MERRA2 Rn in terms of accuracy.

Finally, this study provided an in-depth analysis of the importance of transfer learning inversion factors, especially verifying the key role of shortwave radiation factors in net radiation inversion. Although the generally coarse spatial resolution of currently available meteorological data limited the further refinement of the model, the findings of this study provide directions for future improvements. Specifically, the accuracy and reliability of net radiation inversion can be further improved by improving the meteorological input parameters, optimizing the algorithm, and upgrading the station data.

5. Conclusions

In this study, 25 coarse-resolution (5 km) net radiation models were constructed based on the GLASS Rn product using a transfer learning framework combined with a DenseNet model. By fine-tuning the coarse-resolution model parameters using a small amount of regional surface flux site data, the transfer of the coarse-resolution model of net radiation to the high-resolution (1 km) model was realized. Further, a high-temporal- and spatial-resolution 1 km day-by-day net radiation model was constructed for the Heihe River Basin, which significantly improved the spatial resolution and inversion performance of the net radiation products. The main research results are as follows:

(1) Twenty-five deep-learning net radiation models were pre-trained using the DenseNet model to successfully capture the temporal variations and spatial distribution trends of GLASS net radiation products. The validation accuracies of the optimal net radiation model predictions were achieved with R^2, bias, and root mean square errors of 0.977, 0.1 W/m^2, and 12.004 W/m^2.

(2) The transfer of the coarse-resolution model to the high-resolution model was achieved by parameter fine-tuning using only a small amount of measured flux site net radiation data. The model validation results show that the accurate R^2 and RMSE of the net radiation values predicted by the transfer learning model were improved from 0.839 and 35.741 W/m^2 to 0.924 and 24.292 W/m^2, respectively, compared with the GLASS Rn data.

(3) Among all the covariates, net surface shortwave radiation (SSRA) was considered the most important feature, surface specific humidity (SHU) had the next highest importance, while pressure (PRS), temperature (TEMP), normalized vegetation index (NDVI), and wind speed (WIN) had a relatively small effect on the net radiation prediction.

In this study, a high-spatial-resolution net radiation model based on transfer learning was successfully developed to generate day-by-day net radiation data with 1 km resolution for the Heihe River Basin. The model not only improved the spatial resolution and accuracy of the net radiation data but also significantly reduced the need for ground truth data. This innovative method provides effective technical support for large-scale net radiation inversion, which is of great scientific significance and application value for surface energy balance studies and climate modeling.

Author Contributions: Methodology, S.M. and Q.H.; Validation, S.M.; Formal analysis, S.M.; Data curation, S.M. and Q.H.; Writing—original draft, S.M.; Writing—review and editing, Q.H.; Supervision, S.M., L.Z., Y.G., M.Z. and M.Y.; Project administration, Q.H.; Funding acquisition, Q.H. All authors have read and agreed to the published version of the manuscript.

Funding: This study was supported by the National Key R&D Program of China (grant no. 2021YFB3900601).

Data Availability Statement: The data presented in this study are available upon request from the corresponding author.

Acknowledgments: The authors would like to thank the reviewers and editors for their valuable comments and suggestions.

Conflicts of Interest: The authors declare no conflicts of interest.

References

1. Liang, S.; Wang, D.; He, T.; Yu, Y. Remote sensing of earth's energy budget: Synthesis and review. *Int. J. Digit. Earth.* **2019**, *12*, 737–780. [CrossRef]
2. Dickinson, R.E.; Oleson, K.W.; Bonan, G.; Hoffman, F.; Thornton, P.; Vertenstein, M.; Yang, Z.L.; Zeng, X. The community landmodel and its climate statistics as a component of the community climate system model. *J. Clim.* **2006**, *19*, 2302–2324. [CrossRef]
3. Bisht, G.; Venturini, V.; Islam, S.; Jiang, L. Estimation of the net radiation using modis (moderate resolution imaging spectroradiometer) data for clear sky days. *Remote Sens. Environ.* **2005**, *97*, 52–67. [CrossRef]
4. Liang, S.; Wang, K.; Zhang, X.; Wild, M. Review on estimation of land surface radiation and energy budgets from ground measurement, remote sensing and model simulations. *IEEE J. Sel. Top. Appl. Earth Obs. Remote Sens.* **2010**, *3*, 225–240. [CrossRef]
5. Gao, L.; Zhang, Y.; Zhang, L. Validation and Spatiotemporal Analysis of Surface Net Radiation from CRA/Land and ERA5-Land over the Tibetan Plateau. *Atmosphere* **2023**, *14*, 1542. [CrossRef]
6. Li, S.; Jiang, B.; Peng, J.; Liang, H.; Han, J.; Yao, Y.; Jia, K. Estimation of the All-Wave All-Sky Land Surface Daily Net Radiation at Mid-Low Latitudes from MODIS Data Based on ERA5 Constraints. *Remote Sens.* **2022**, *14*, 33. [CrossRef]
7. Meng, C. Review of Numerical Simulation Research on Urban Land Surface Characteristics. *Adv. Earth Sci.* **2014**, *29*, 464–474.
8. Urraca, R.; Huld, T.; Gracia-Amillo, A.; Martinez-de-Pison, F.J.; Kaspar, F.; Sanz-Garcia, A. Evaluation of global horizontal irradiance estimates from ERA5 and COSMO-REA6 reanalyses using ground and satellite-based data. *Sol. Energy* **2018**, *164*, 339–354. [CrossRef]
9. Decker, M.; Brunke, M.A.; Wang, Z.; Sakaguchi, K.; Zeng, X.; Bosilovich, M.G. Evaluation of the reanalysis products from GSFC, NCEP, and ECMWF using flux tower observations. *J. Clim.* **2012**, *25*, 1916–1944. [CrossRef]
10. Jia, A.; Liang, S.; Jiang, B.; Zhang, X.; Wang, G. Comprehensive Assessment of Global Surface Net Radiation Products and Uncertainty Analysis. *J. Geophys. Res. Atmos.* **2018**, *123*, 1970–1989. [CrossRef]
11. Wild, M.; Folini, D.; Schär, C.; Loeb, N.; Dutton, E.G.; König-Langlo, G. The global energy balance from a surface perspective. *Clim. Dyn.* **2012**, *40*, 3107–3134. [CrossRef]
12. Liu, K.; Wu, X.; Liu, Y.; Ali, M.; Yang, F.; He, Q. Estimation of hourly surface net radiation in Taklimakan Desert based on multi-source remote sensing data and reanalysis data. *J. Desert Res.* **2021**, *41*, 51–61.
13. Chen, J.; He, T.; Jiang, B.; Liang, S. Estimation of all-sky all-wave daily net radiation at high latitudes from MODIS data. *Remote Sens. Environ.* **2020**, *245*, 111842. [CrossRef]
14. Amatya, P.M.; Ma, Y.; Han, C.; Wang, B.; Devkota, L.P. Estimation of net radiation flux distribution on the southern slopes of the central Himalayas using MODIS data. *Atmos. Res.* **2015**, *154*, 146–154. [CrossRef]
15. Tegegne, E.B.; Ma, Y.; Chen, X.; Ma, W.; Wang, B.; Ding, Z.; Zhu, Z. Estimation of the distribution of the total net radiative flux from satellite and automatic weather station data in the Upper Blue Nile basin, Ethiopia. *Theor. Appl. Climatol.* **2020**, *143*, 587–602. [CrossRef]
16. Banerjee, S.; Singal, G.; Saha, S.; Mittal, H.; Srivastava, M.; Mukherjee, A.; Garg, D. Machine Learning approach to Predict net radiation over crop surfaces from global solar radiation and canopy temperature data. *Int. J. Biometeorol.* **2022**, *66*, 2405–2415. [CrossRef] [PubMed]
17. Jiang, B.; Zhang, Y.; Liang, S.; Zhang, X.; Xiao, Z. Surface Daytime Net Radiation Estimation Using Artificial Neural Networks. *Remote Sen.* **2014**, *6*, 11031–11050. [CrossRef]
18. Ojo, O.S.; Adeyemi, B.; Oluleye, D.O. Artificial neural network models for prediction of net radiation over a tropical region. *Neural Comput. Appl.* **2021**, *33*, 6865–6877. [CrossRef]
19. Jia, L.; Su, Z.; Hurk, D.V.; Moene, A.F.; Menenti, M. The surface energy balance system (SEBS) for estimating energy balance at regional scale—A validation using atsr and scintillometer measurements and RACMO PBL variables. *Assoc. Coll. Res. Libr. Am. Libr. Assoc.* **2002**, *23*, 8–9.
20. Zeng, Z.; Li, Z.; Luo, X.; Li, X. Estimation of surface net radiation using a deep learning approach. *J. Hydrol.* **2019**, *575*, 124001.
21. Li, X.; Li, Z.; Zeng, C.; Wang, J. A machine learning-based data fusion approach for estimating surface net radiation in the Tibetan Plateau. *Remote Sens.* **2020**, *12*, 341.
22. Wang, K.; Li, X.; Li, Z. Estimation of terrestrial surface net radiation using a deep learning model. *Remote Sens.* **2021**, *13*, 154.
23. Liu, Y.; Li, X.; Li, Z.; Tang, W. Estimation of surface net solar radiation using a machine learning model and its application in a water-energy balance model. *Remote Sens.* **2022**, *14*, 403.
24. Zhang, Y.; Li, X.; Li, Z. A deep learning-based method for estimating surface net radiation from remote sensing data. *Remote Sens.* **2021**, *13*, 3042.
25. Hemmati, E.; Sahebi, M.R. Surface soil moisture retrieval based on transfer learning using SAR data on a local scale. *Int. J. Remote Sens.* **2024**, *45*, 2374–2406. [CrossRef]
26. Zhu, L.; Dai, J.; Liu, Y.; Yuan, S.; Qin, T.; Walker, J.P. A cross-resolution transfer learning approach for soil moisture retrieval from Sentinel-1 using limited training samples. *Remote Sens. Environ.* **2024**, *301*, 113944. [CrossRef]
27. Saha, S. The NCEP Climate Forecast System Reanalysis. *Bull. Am. Meteorol. Soc.* **2010**, *91*, 1015–1057. [CrossRef]
28. Rienecker, M.M.; Suarez, M.J.; Gelaro, R. MERRA: NASA's Modern-Era Retrospective Analysis for Research and Applications. *J. Clim.* **2011**, *24*, 3624–3648. [CrossRef]
29. Simmons, A.J.; Gibson, J.K. *ERA-40 Project Report Series. 1. The ERA-40 Project Plan*; ECMWF: Reading, UK, 2020; 62p.

30. Berrisford, P.; Kållberg, P.; Kobayashi, S.; Dee, D.; Uppala, S.; Simmons, A.J.; Sato, H. Atmospheric conservation properties in ERA-Interim. *Q. J. R. Meteorol. Soc.* **2011**, *137*, 1381–1399. [CrossRef]
31. Young, D.F.; Wong, T.; Wielicki, B.A. Temporal Interpolation Methods for the Clouds and the Earth's Radiant Energy System (CERES) Experiment. *J. Appl. Meteor. Climatol.* **1998**, *37*, 572–590. [CrossRef]
32. Zhang, Y.C.; Rossow, W.B.; Lacis, A.A. Calculation of surface and top of atmosphere radiative fluxes from physical quantities based on ISCCP data sets: 2.Validation and first result. *J. Geophys. Res. Atmos.* **1995**, *100*, 1167–1197. [CrossRef]
33. Liu, S.; Li, X.; Xu, Z.; Che, T.; Xiao, Q.; Ma, M.; Ren, Z. The Heihe Integrated Observatory Network: A Basin-scale Land Surface Processes Observatory in China. *Vadose Zone J.* **2018**, *17*, 1–21. [CrossRef]
34. Li, X.; Liu, S.; Xiao, Q.; Ma, M.; Jin, R.; Che, T.; Wang, L. A multiscale dataset for understanding complex eco-hydrological processes in a heterogeneous oasis system. *Sci. Data* **2017**, *4*, 170083. [CrossRef] [PubMed]
35. Jiang, B.; Liang, S.; Jia, A.; Xu, J.; Zhang, X.; Xiao, Z.; Yao, Y. Validation of the surface daytime net radiation product from version 4.0 GLASS product suite. *IEEE Geosci. Remote Sens. Lett.* **2018**, *16*, 509–513. [CrossRef]
36. Schotanus, P.; Nieuwstadt, F.; De Bruin, H.A.R. Temperature-Measurement with a Sonic Anemometer and Its Application to Heat and Moisture Fluxes. *Bound. Layer Meteorol.* **1983**, *26*, 81–93. [CrossRef]
37. Moore, C.J. Frequency response corrections for eddy correlation systems. *Bound. Layer Meteorol.* **1986**, *37*, 17–35. [CrossRef]
38. Huang, G.; Liu, Z.; Pleiss, G.; Van Der Maaten, L.; Weinberger, K.Q. Convolutional networks with dense connectivity. *IEEE Trans. Pattern Anal. Mach. Intell.* **2019**, *44*, 8704–8716. [CrossRef] [PubMed]
39. Aljazaeri, M.; Bazi, Y.; AlMubarak, H.; Alajlan, N. Faster R-CNN and DenseNet regression for glaucoma detection in retinal fundus images. In Proceedings of the 2020 2nd International Conference on Computer and Information Sciences (ICCIS), Sakaka, Saudi Arabia, 13–15 October 2020; pp. 1–4.
40. Eldan, R.; Shamir, O. The power of depth for feedforward neural networks. In Proceedings of the Conference on Learning Theory, PMLR, New York, NY, USA, 23–26 June 2016; pp. 907–940.
41. Wu, Z.; Shen, C.; Van Den Hengel, A. Wider or deeper: Revisiting the resnet model for visual recognition. *Pattern Recognit.* **2019**, *90*, 119–133. [CrossRef]
42. Entekhabi, D.; Reichle, R.H.; Koster, R.D.; Crow, W.T. Performance metrics for soil moisture retrievals and application requirements. *J. Hydrometeorol.* **2010**, *11*, 832–840. [CrossRef]
43. Wang, Y.; Jiang, B.; Liang, S.; Wang, D.; He, T.; Wang, Q.; Zhao, X.; Xu, J. Surface Shortwave Net Radiation Estimation from Landsat TM/ETM+ Data Using Four Machine Learning Algorithms. *Remote Sens.* **2019**, *11*, 2847. [CrossRef]
44. Guo, Y.; Cheng, J. Feasibility of estimating cloudy-sky surface longwave net radiation using satellite-derived surface shortwave net radiation. *Remote Sen.* **2018**, *10*, 596. [CrossRef]
45. Gusain, H.S.; Singh, D.K.; Mishra, V.D.; Arora, M.K. Estimation of net radiation flux of antarctic ice sheet in East dronning Maud land, Antarctica, during clear sky days using remote sensing and meteorological data. *Remote Sens. Earth Syst. Sci.* **2018**, *1*, 89–99. [CrossRef]
46. Seyednasrollah, B.; Kumar, M.; Link, T.E. On the role of vegetation density on net snow cover radiation at the forest floor. *J. Geophys. Res. Atmos.* **2013**, *118*, 8359–8374. [CrossRef]
47. Seyednasrollah, B.; Kumar, M. Effects of tree morphometry on net snow cover radiation on forest floor for varying vegetation densities. *J. Geophys. Res. Atmos.* **2013**, *118*, 12508–12521. [CrossRef]
48. Xu, J.; Liang, S.; Ma, H.; He, T.; Zhang, Y.; Zhang, G. A daily 5-km all-sky sea-surface longwave radiation product based on statistically modified deep neural network and spatiotemporal analysis for 1981–2018. *Remote Sens. Environ.* **2023**, *290*, 113550. [CrossRef]
49. Hu, A.F.; Xie, S.L.; Li, T. Soil parameter inversion modeling using deep learning algorithms and its application to settlement prediction: A comparative study. *Acta Geotech.* **2023**, *18*, 5597–5618. [CrossRef]
50. Pan, S.J.; Yang, Q. A survey on transfer learning. *IEEE Trans. Knowl. Data Eng.* **2010**, *22*, 1345–1359. [CrossRef]
51. Zhuang, F.; Qi, Z.; Duan, K.; Xi, D.; Zhu, Y.; He, Q. A Comprehensive Survey on Transfer Learning. *Proc. IEEE* **2021**, *109*, 43–76. [CrossRef]
52. Verma, N.; Maurya, S.P.; Kant, R. Comparison of neural networks techniques to predict subsurface parameters based on seismic inversion: A machine learning approach. *Earth Sci. Inform.* **2024**, *17*, 1031–1052. [CrossRef]
53. Rainio, O.; Teuho, J.; Klén, R. Evaluation metrics and statistical tests for machine learning. *Sci. Rep.* **2024**, *14*, 6086. [CrossRef] [PubMed]
54. Jiang, B.; Zhang, Y.; Liang, S.; Wohlfahrt, G.; Arain, A.; Cescatti, A.; Georgiadis, T.; Jia, K.; Kiely, G.; Lund, M.; et al. Empirical estimation of daytime net radiation from shortwave radiation and ancillary information. *Agric. For. Meteorol.* **2015**, *211*, 23–36. [CrossRef]
55. Guo, X.; Yao, Y.; Zhang, Y.; Lin, Y.; Jiang, B.; Jia, K.; Zhang, X.; Xie, X.; Zhang, L.; Shang, K.; et al. Discrepancies in the simulated global terrestrial latent heat flux from glass and merra-2 surface net radiation products. *Remote Sens.* **2020**, *12*, 2763. [CrossRef]